4-1-2013

Direct EIT Reconstructions of Complex Admittivities on a Chest-Shaped Domain in 2-D

Sarah J. Hamilton
Marquette University, sarah.hamilton@marquette.edu

Jennifer L. Mueller
Colorado State University

Accepted version. *IEEE Transactions on Medical Imaging*, Vol. 32, No. 4 (April 2013): 757-769. DOI.

Sarah Hamilton was affiliated with Colorado State University at the time of publication.

IEEE Transactions on Medical Imaging, Vol. 32, No. 4 (April 2013): 757-769. DOI.

Direct EIT Reconstructions of Complex Admittivities on a Chest-Shaped Domain in 2-D

Sarah J. Hamilton
Department of Mathematics, Colorado State University, Fort Collins, CO
Jennifer L. Mueller
Department of Mathematics and School of Biomedical Engineering, Colorado State University, Fort Collins, CO

Abstract:

Electrical impedance tomography (EIT) is a medical imaging technique in which current is applied on electrodes on the surface of the body, the resulting voltage is measured, and an inverse problem is solved to recover the conductivity and/or permittivity in the interior. Images are then formed from the reconstructed conductivity and permittivity distributions. In the 2-D geometry, EIT is clinically useful for chest imaging. In this work, an implementation of a D-bar method for complex admittivities on a general 2-D domain is presented. In particular, reconstructions are computed on a chest-shaped domain for several realistic phantoms including a simulated pneumothorax, hyperinflation, and pleural effusion. The method demonstrates robustness in the presence of noise. Reconstructions from trigonometric and pairwise current injection patterns are included.

Keywords

Electrodes, Image reconstruction, Conductivity, Voltage measurement, Permittivity, Reconstruction algorithms

SECTION I.

Introduction

Electrical impedance tomography (EIT) is a relatively new imaging technique based on the fact that the electrical conductivity and permittivity vary in the different tissues and organs in the body, allowing one to form images from the reconstructed conductivity and permittivity distributions. In the 2-D geometry, EIT is clinically useful for chest imaging. Conductivity images have been used for monitoring pulmonary perfusion [5], [20], [44], determining regional ventilation in the lungs [19], [21], [49], detecting extravascular lung water [36], and evaluating shifts in lung fluid in congestive heart failure patients [18]. Regional results have been validated with CT images [12], [20], [21], [44] and radionuclide scanning [35] in the presence of pathologies such as atelectasis, pleural effusion, and pneumothorax.

In EIT, data is collected on electrodes placed around the perimeter of a patient's chest, and a reconstruction algorithm is used to compute the admittivity $\gamma(x,y) = \sigma(x,y) + i\omega\epsilon(x,y)$ in the plane of the electrodes. Here, σ is the conductivity of the medium, ϵ is the permittivity, and ω is the temporal angular frequency of the applied electromagnetic wave. Most data acquisition systems and algorithms compute the real part of γ, that is, the conductivity. However, computing the permittivity component provides an additional image that may have clinical usefulness in distinguishing between certain conditions such as a pneumothorax and hyperinflation. Both of these conditions correspond to a low resistivity region, but the pneumothorax has zero permittivity while hyperinflation has low, nonzero permittivity.

If the EIT image depicts changes in admittivity relative to another measured data set, the reconstruction is called a *difference image*. If the image represents an estimate of the actual admittivity values at each pixel in the domain of interest, it is called an *absolute image*.

Here, we consider a direct reconstruction algorithm developed in [24] that reconstructs a complex admittivity without iteration from several integral equations. The algorithm in [24] is the first D-bar method for the reconstruction of admittivities in two dimensions. The framework is based on the uniqueness proof in [17], but equations relating the Dirichlet-to-Neumann map to the scattering transform and the exponentially growing solutions are not present in that work, and are derived in [24].

Reconstruction algorithms for complex admittivities based on an iterative least-squares approach are found in [4], [15], [30] and an iterative package for 3-D reconstructions has been published in [42]. Another approach to the inverse problem is that of shape-based reconstruction methods for determining the location and shape of inclusions in the plane of the electrodes. Results from such methods can be used as priors or constraints in iterative approaches. Level-set methods for shape-based EIT reconstructions of conductivity include [1], [8], and [14]. The enclosure method was introduced in [25] and implemented (independently) in [6] and [26]. See, for example, [3] and [37] for a review of reconstruction algorithms for EIT.

The work presented here is a direct method that makes use of exponentially growing solutions, or complex geometrical optics (CGO) solutions, to the admittivity equation. The steps of the algorithm are to compute these CGO solutions from knowledge of the Dirichlet-to-Neumann map, compute a scattering transform matrix, solve two systems of $\bar{\partial}$ (D-bar) equations in the complex frequency variable k for the CGO solutions to a related elliptic system, and finally to reconstruct the admittivity distribution from the values of these related CGO solutions at $k = 0$.

In this paper, we extend the implementation to noncircular domains, focusing on technical aspects of the implementation not included in [24], and we demonstrate the good spatial resolution and accuracy of the algorithm on simulated examples of clinical interest. Absolute images and difference images of simulated pleural effusion, pneumothorax, and hyperinflation are presented, three conditions for which it would be beneficial to clinicians to be able to image in the ICU. To take into account various types of EIT hardware, we consider two types of applied current patterns in this work: trigonometric current patterns, in which current is applied simultaneously on all electrodes, and adjacent current patterns, in which only one pair of neighboring electrodes is active in each data acquisition set. We consider data with several noise levels and demonstrate that the algorithm is reasonably robust.

A theory for full nonlinear reconstructions of permittivities in 3-D by a direct method does not yet exist, and while this method is not immediately generalizable to three dimensional reconstructions, 2-D reconstructions are useful, for instance, for imaging patients in the ICU under mechanical ventilation [12].

This paper is organized as follows. In Section II we describe the simulation of the data and finite-dimensional approximation of the Dirichlet-to-Neumann map. In Section III, the direct D-bar reconstruction algorithm is briefly described. Details of the implementation are provided in Section IV. The absolute images and difference images of simulated pleural effusion, pneumothorax, and hyperinflation are found in Section V.

SECTION II.

Measurement and Simulation

The reconstruction algorithm requires knowledge of the Dirichlet-to-Neumann map (DN map), or voltage-to-current density map. In this section we describe the map mathematically and explain how a finite-dimensional matrix approximation is computed from data simulated by the finite element method (FEM).

The reconstruction of admittivies $\gamma(x, y) = \sigma(x, y) + i\omega\epsilon(x, y)$ from electrical boundary measurements is known as the *inverse admittivity problem*. The propagation of electromagnetic fields within the body is governed by Maxwell's equations. The application of time-harmonic currents and the electromagnetic properties of the human body facilitate reducing the model to the generalized Laplace equation

$$\nabla \cdot (\gamma(x, y)\nabla u(x, y)) = 0, (x, y) \in \Omega \quad (1)$$

where Ω denotes a bounded region in the plane, and u denotes the electric potential. See, for example, [27] and [37] for details of this calculation.

Applying a known voltage on the boundary of Ω corresponds to the Dirichlet boundary condition

$$u(x,y) = f(x,y), (x,y) \in \partial\Omega \quad (2)$$

where $\partial\Omega$ denotes the boundary of Ω, and knowledge of the resulting current density distribution on the boundary gives rise to the Neumann boundary condition

$$\gamma(x,y)\frac{\partial u}{\partial \nu}(x,y) = j(x,y) \quad (3)$$

where ν denotes the outward unit normal to $\partial\Omega$. The mapping which takes a given voltage distribution on the boundary to the resulting current density distribution on the boundary is referred to as the Dirichlet-to-Neumann (DN), or voltage-to-current density, map and is denoted by Λ_γ. Since the physical interpretation of Λ_γ is knowledge of the resulting current distributions on the boundary of Ω corresponding to all possible voltage distributions on the boundary, it can be viewed as our data. In practice, current is applied on the electrodes and the resulting voltage is measured. This map, the Neumann-to-Dirichlet (ND) map, is denoted by R_γ. The DN map is the inverse of the ND map. The finite-dimensional matrix approximations to Λ_γ and R_γ will be denoted by Λ_γ^M and R_γ^M, respectively. When the admittivity is the constant value of 1 in Ω, the corresponding DN map will be denoted by Λ_1. We will need the difference of DN maps, $\Lambda_\gamma - \Lambda_1$ in the forthcoming formulas, and we will denote this difference by $\delta\Lambda_\gamma$ and the finite-dimensional matrix approximation to the difference by $\delta\Lambda_\gamma^M$.

We consider two choices of current patterns in our simulations. The first are the trigonometric patterns, $1 \le \ell \le L$

$$T_\ell^j = \begin{cases} C\cos(j\theta_\ell), & 1 \le \ell \le L, 1 \le j \le \frac{L}{2} \\ C\sin((\frac{L}{2} - j)\theta_\ell), & 1 \le \ell \le L, \frac{L}{2} + 1 \le j \le L-1 \end{cases} \quad (4)$$

where L denotes the total number of electrodes, $\theta_\ell = 2\pi\ell/L$, and T_ℓ^j is the current on the ℓth electrode corresponding to the jth current pattern. The second is the adjacent current pattern, a pairwise activation pattern

$$T_\ell^j = \begin{cases} C, & \ell = j, j = 1, \dots, L-1 \\ -C, & \ell = j+1, j = 1, \dots, L-1 \\ 0, & \text{otherwise.} \end{cases} \quad (5)$$

Notice that in each case there are $L-1$ linearly independent current patterns, and the voltage values are “measured” on all L electrodes.

The Complete Electrode Model (CEM) consists of the PDE (1) and boundary conditions that take into account both the shunting effect of the electrodes and the contact impedances between the electrodes and tissue. The CEM is well-studied in the EIT literature and the reader is referred to [7], [45], [48] for further details on the equations and their implementation into the FEM. Here, voltage data on $L = 32$ electrodes was simulated with the CEM and implemented with the finite

element method. The FEM computations were performed on the chest-shaped domain with perimeter 900 mm and 32 equispaced electrodes of length 0.029 m placed on the boundary. The effective contact impedance was chosen to be $z = 10^{-8}\Omega\text{-m}^2$ on all electrodes in our simulations. The current amplitude was chosen to be $C = 2\text{mA}$.

Where indicated, Gaussian relative noise was added to the simulated voltages as follows. Denote the (complex-valued) vector of computed voltages for the jth current pattern by V^j, let η denote the noise level, and N^j a Gaussian random vector (generated by the randn command in MATLAB) that is unique for each current pattern j. Denoting the noisy data by $\tilde{V}^j$, we then have $\tilde{V}^j = \text{Re}(\tilde{V}^j) + i\text{Im}(\tilde{V}^j)$ where

$$\begin{aligned}\text{Re}(\tilde{V}^j) &= \text{Re}(V^j) + \eta max|\text{Re}(V^j)|N^j \\ \text{Im}(\tilde{V}^j) &= \text{Im}(V^j) + \eta max|\text{Im}(V^j)|N^j.\end{aligned}$$

The map Λ_γ^M was then computed as in [28] and [29], which we summarize briefly here. Let Φ_ℓ^j denote the (ℓ, j)th entry of the matrix of applied currents with each column normalized with respect to the l^2-vector norm. That is, $\Phi_\ell^j = T^j / \| T^j \|_2$. Let v_ℓ^j denote the entries of the jth voltage vector normalized so that $v_\ell^j = V_\ell / \| T^j \|_2$. Let $|e_\ell|$ denote the area of the ℓth electrode. Then $\Lambda_\gamma^M = (R_\gamma^M)^{-1}$ where the (m, n)th entry of R_γ^M is given by

$$R_\gamma^M(m,n) := \gamma_0 \sum_{\ell=1}^{L} \frac{1}{|e_\ell|} \Phi_\ell^m v_\ell^n. \quad (6)$$

SECTION III.

Description of the Algorithm

In the mathematical formulation of the reconstruction algorithm, we require special, nonphysical, exponentially growing solutions to (1), which are realized by introducing a nonphysical complex frequency parameter k, and extending (1) to the entire plane under the assumption that γ is constant in a neighborhood of the boundary of Ω. This assumption can be imposed in practice by assuming that near the boundary, γ is the best constant admittivity γ_0 approximation to the measured data. Having found γ_0, the admittivity can be scaled by $\tilde{\gamma} = \gamma/\gamma_0$ and the DN map can be scaled accordingly by $\Lambda_{\tilde{\gamma}} = \gamma_0 \Lambda_\gamma$. With this scaling, γ is then recovered at the end by $\gamma = \gamma_0 \tilde{\gamma}$. See [46] for a treatment of the case of a nonconstant boundary conductivity for the real-valued D-bar method. In the remainder of this paper, we will identify a point $(x, y) \in \mathbb{R}^2$ with the complex number $z = x + iy$, and thus the multiplication kz denotes complex multiplication $kz = (k_1 + ik_2)(x + iy)$. The nonphysical exponentially growing solutions u_j satisfy

$$\nabla \cdot (\gamma(z) \nabla u_j(z,k)) = 0, z \in \Omega, k \in \mathbb{C}, j = 1,2 \quad (7)$$

where $u_1 \sim e^{ikz}/(ik)$ and $u_2 \sim e^{-ik\overline{z}}/(-ik)$ in a sense that is made precise in [24]. The existence of such solutions is established in [24] and [50] where boundary integral equations in terms of the DN maps are presented. These solutions are the key connection between the CGO solutions and the measured data and satisfy the following boundary integral equations for $z \in \partial\Omega$:

$$\begin{aligned} u_1(z,k) = \quad & \frac{e^{ikz}}{ik} - \int_{\partial\Omega} G_k(z-\zeta)\delta\Lambda_\gamma u_1(\zeta,k)dS(\zeta) \\ u_2(z,k) = \quad & \frac{e^{-ik\overline{z}}}{-ik} \\ & - \int_{\partial\Omega} G_k(-\overline{z}+\overline{\zeta})\delta\Lambda_\gamma u_2(\zeta,k)dS(\zeta) \end{aligned} \quad (8)(9)$$

where $G_k(z)$ is a special Green's function for the Laplacian known as the Faddeev Green's function [16]. It is defined by

$$G_k(z) := e^{ikz} g_k(z), -\Delta G_k = \delta \ (10)$$

where

$$g_k(z) := \frac{1}{(2\pi)^2} \int_{\mathbb{R}^2} \frac{e^{iz\cdot\xi}}{\xi(\overline{\xi}+2k)} d\xi, (-\Delta - 4ik\,\overline{\partial}) g_k = \delta \ (11)$$

for $k \in \mathbb{C} \setminus \{0\}$, where $z \cdot \xi = x\xi_1 + y\xi_2, \xi = \xi_1 + i\xi_2$.

A second type of CGO solution is required for the mathematical reconstruction algorithm. These solutions were introduced in [17], and involve formulating the problem as an elliptic system. Define $Q_\gamma(z)$ as a transformation of γ and a matrix operator D by

$$\begin{aligned} Q_\gamma(z) = \quad & \begin{pmatrix} 0 & -\frac{1}{2}\partial_z \log\gamma(z) \\ -\frac{1}{2}\overline{\partial}_z \log\gamma(z) & 0 \end{pmatrix} \\ D = \quad & \begin{pmatrix} \overline{\partial}_z & 0 \\ 0 & \partial_z \end{pmatrix}. \end{aligned} \quad (12)$$

Defining a vector $\vec{v} = (v_1, v_2)^T = \gamma^{1/2}(\partial_z u, \overline{\partial}_z u)^T$ in terms of the solution u to (1), one sees that $D\vec{v} - Q_\gamma \vec{v} = 0$.

Francini shows in [17] that for ω sufficiently small, $\sigma(z) > \sigma_0 > 0$, and $\| \sigma \|_{W^{1,\infty}(\Omega)}, \| \epsilon \|_{W^{1,\infty}(\Omega)} \leq \beta$, there exists a unique 2×2 matrix $\Psi(z,k)$ for $k \in \mathbb{C}$ that is a solution to

$$\Big(D - Q_\gamma(z)\Big)\Psi(z,k) = 0$$

with $\Psi_{12}, \Psi_{21} \sim 0, \Psi_{11} \sim e^{ikz}$ and $\Psi_{21} \sim e^{-ik\bar{z}}$ where the asymptotic condition is made precise in [17]. The columns of Ψ serve as two such vectors $\vec{v}$ separately satisfying

$$\begin{pmatrix}\Psi_{11}\\ \Psi_{21}\end{pmatrix} = \gamma^{1/2}\begin{pmatrix}\partial_z u_1\\ \overline{\partial}_z u_1\end{pmatrix}, \begin{pmatrix}\Psi_{12}\\ \Psi_{22}\end{pmatrix} = \gamma^{1/2}\begin{pmatrix}\partial_z u_2\\ \overline{\partial}_z u_2\end{pmatrix}.$$

The values of u_1 and u_2 on $\partial\Omega$ are related to the off-diagonal entries of Ψ on $\partial\Omega$ through the boundary integrals [23]

$$\begin{aligned}\Psi_{12}(z,k) = &\int_{\partial\Omega} \frac{e^{i\bar{k}(z-\zeta)}}{4\pi(z-\zeta)}\delta\Lambda_\gamma u_2(\zeta,k)dS(\zeta)\\ \Psi_{21}(z,k) = &\int_{\partial\Omega} \overline{\left[\frac{e^{ik(z-\zeta)}}{4\pi(z-\zeta)}\right]}\delta\Lambda_\gamma u_1(\zeta,k)dS(\zeta).\end{aligned} \quad (14)(15)$$

As in other D-bar algorithms, [2], [34] the admittivity can be reconstructed directly from knowledge of the CGO solutions. Equation (16) follows directly from formulas in [23], [24]

$$\gamma(z) = \exp\left(-\frac{2}{\pi}\int_{\mathbb{C}} \frac{1}{z-\zeta}\frac{\partial_\zeta M_-(\zeta,0)}{M_+(\zeta,0)}d\zeta\right) \quad (16)$$

where

$$\begin{aligned}M_+(z,k) = &\quad M_{11}(z,k) + e^{-i(kz+\bar{k}\bar{z})}M_{12}(z,k)\\ M_-(z,k) = &\quad M_{22}(z,k) + e^{i(kz+\bar{k}\bar{z})}M_{21}(z,k)\end{aligned} \quad (17)(18)$$

and the matrix of CGO solutions $M(z,k)$ are related to $\Psi(z,k)$ via

$$M(z,k) = \Psi(z,k)\begin{pmatrix}e^{-izk} & 0\\ 0 & e^{i\bar{z}k}\end{pmatrix}. \quad (19)$$

The values of the CGO solutions $M(z,0)$ are found by solving the following D-bar equation, in the kvariable, derived in [17]

$$\overline{\partial}_k M(z,k) = M(z,\bar{k})\begin{pmatrix}e^{i(\bar{k}z+k\bar{z})} & 0\\ 0 & e^{-i(kz+\bar{k}\bar{z})}\end{pmatrix}S_\gamma(k) \quad (20)$$

for $M(z,k)$ and evaluating at $k=0$. $S_\gamma(k)$ is called the *scattering transform matrix*, a matrix with diagonal entries of 0 and off-diagonal entries defined by

$$\begin{aligned}S_{12}(k) = &\quad \frac{i}{\pi}\int_\Omega Q_{12}(z)e^{-i\bar{k}z}\Psi_{22}(z,k)d\mu(z)\\ S_{21}(k) = &\quad -\frac{i}{\pi}\int_\Omega Q_{21}(z)e^{i\bar{k}\bar{z}}\Psi_{11}(z,k)d\mu(z).\end{aligned} \quad (21)(22)$$

Integrating (21) and (22) by parts results in formulas for S_{12} and S_{21} in terms of the boundary values of Ψ

$$S_{12}(k) = \frac{i}{2\pi}\int_{\partial\Omega} e^{-i\bar{k}z}\Psi_{12}(z,k)(v_1 + iv_2)dS(z)$$
$$S_{21}(k) = -\frac{i}{2\pi}\int_{\partial\Omega} e^{i\bar{k}\bar{z}}\Psi_{21}(z,k)(v_1 - iv_2)dS(z) \quad (23)(24)$$

illustrating the necessity of only the boundary values of the CGO solutions Ψ_{12} and Ψ_{21} rather than their solutions in all of $\mathbb{R}^2$.

This completes the set of equations necessary to directly determine γ from Λ_γ. We clarify these steps in Fig.1.

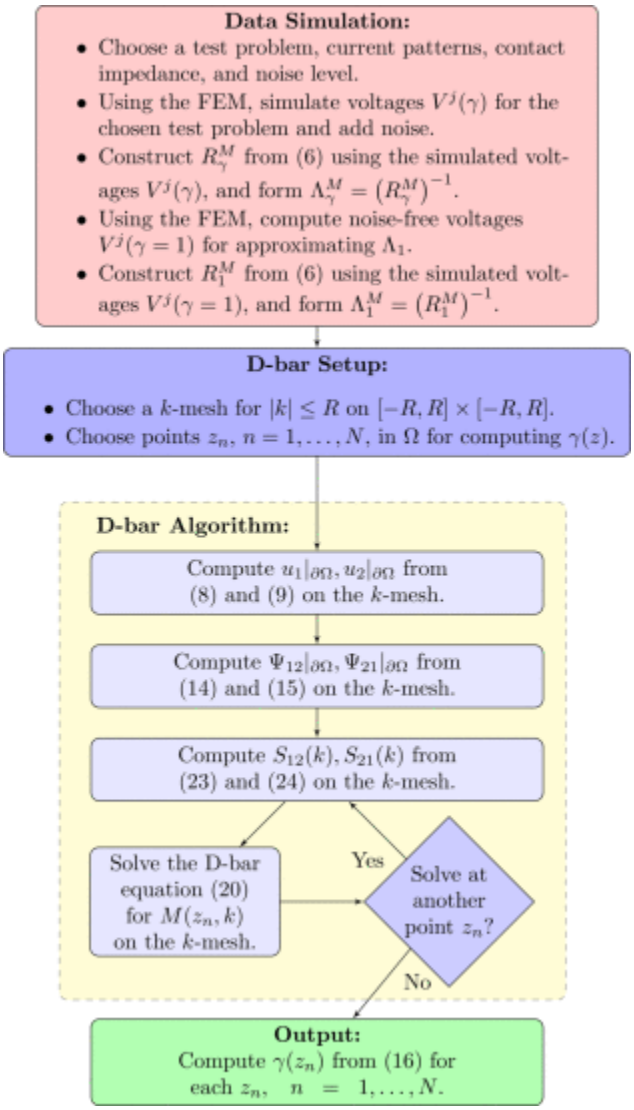

Fig. 1. Flowchart describing the algorithm.

SECTION IV.

Implementation Details

The first three steps in the algorithm involve computing integrals over the boundary of the domain. When the computation involves the DN map, the boundary is discretized in terms of the centers of the L electrodes, since our electrode model assumes the voltages are constant on each electrode. We denote the center of the ℓth electrode by $z_\ell, \ell = 1, \ldots, L$.

A. Computation of the CGO Solutions

The boundary integrals (8) and (9) for u_1 and u_2, respectively, on the boundary of the chest-shaped domain were computed as follows. The normalized basis functions Φ_ℓ^j (4) cannot be used to accurately approximate a constant function, and so we modify equations (8) and (9), making use of the fact that $\delta\Lambda_\gamma(1/(ik)) = 1/(ik)\delta\Lambda_\gamma(1) = 0$, and write (8) and (9) in the equivalent forms for $\tilde{u}_1(z,k) := u_1(z,k) - 1/ik$, $\tilde{u}_2(z,k) := u_2(z,k) + 1/ik$

$$\begin{aligned} \tilde{u}_1(z,k) = \quad & e^1(z,k) \\ & - \int_{\partial\Omega} G_k(z-\zeta)\delta\Lambda_\gamma \tilde{u}_1(\zeta,k)dS(\zeta) \\ \tilde{u}_2(z,k) = \quad & e^2(z,k) \\ & - \int_{\partial\Omega} G_k(-\overline{z}+\overline{\zeta})\delta\Lambda_\gamma \tilde{u}_2(\zeta,k)dS(\zeta) \end{aligned} \qquad (25)(26)$$

where $e^1(z,k) := e^{ikz}/ik - 1/ik$ and $e^2(z,k) := e^{-ik\overline{z}}/-ik + 1/ik$.

Equations (25) and (26) were solved for k values on a disk $|k| \leq R$ independently for each k as follows (note that this step can be performed in parallel). The functions $\tilde{u}_1(z,k)$, $\tilde{u}_2(z,k)$, $e^1(z,k)$ and $e^2(z,k)$ restricted to the boundary were expanded in the normalized basis functions Φ_ℓ^j and evaluated at the boundary points z_ℓ

$$\begin{aligned} \tilde{u}_1(z_\ell,k) \approx \quad & \sum_{j=1}^{L-1} b_j^1(k)\Phi_\ell^j \\ \tilde{u}_2(z_\ell,k) \approx \quad & \sum_{j=1}^{L-1} b_j^2(k)\Phi_\ell^j \\ e_\ell^1(k) = \quad & \sum_{j=1}^{L-1} c_j^1(k)\Phi_\ell^j \\ e_\ell^2(k) = \quad & \sum_{j=1}^{L-1} c_j^2(k)\Phi_\ell^j. \end{aligned} \qquad (27)(28)$$

Let $\mathbf{b^1}(k)$ denote the column vector $\mathbf{b^1}(k) = [b_1^1(k), \ldots, b_{L-1}^1(k)]^T$, and define $\mathbf{b^2}(k)$, $\mathbf{c^1}(k)$ and $\mathbf{c^2}(k)$ analogously.

Let $E_{\ell'}$ denote the ℓ'th subdivision of the boundary ($\ell' = 1, \dots, L$) centered at $z_{\ell'}$ with length P/L, where P denotes the perimeter of the domain. Splitting the integral over $\partial\Omega$ into a sum of integrals over the subsections $E_{\ell'}$

$$\begin{aligned}\widetilde{u}_1(z_\ell, k) \approx \quad & e^1(z_\ell, k) \\ & - \sum_{\ell'=1}^{L} \int_{E_{\ell'}} G_k(z_\ell - \zeta) \delta\Lambda_\gamma^M \widetilde{u}_1(\cdot, k)|_{\zeta_{\ell'}} dS(\zeta) \\ = \quad & e^1(z_\ell, k) \\ & - \sum_{\ell'=1}^{L} \int_{E_{\ell'}} G_k(z_\ell - \zeta) dS(\zeta) [\delta\Lambda_\gamma^M \widetilde{u}_1(\zeta_{\ell'}, k)].\end{aligned}$$

Using the expansions for $\widetilde{u}_1$ and e^1, (27) and (28), respectively, we have

$$\begin{aligned}& \sum_{j=1}^{L-1} b_j^1(k) \Phi_\ell^j \\ & \approx \sum_{j=1}^{L-1} c_j^1(k) \Phi_\ell^j \\ & - \sum_{\ell'=1}^{L} \int_{E_{\ell'}} G_k(z_\ell - \zeta) dS(\zeta) \left[\delta\Lambda_\gamma^M \sum_{j=1}^{L-1} b_j^1(k) \Phi_{\ell'}^j \right] \\ & = \sum_{j=1}^{L-1} c_j^1(k) \Phi_\ell^j \\ & - \sum_{\ell'=1}^{L} \int_{E_{\ell'}} G_k(z_\ell - \zeta) dS(\zeta) \sum_{j=1}^{L-1} b_j^1(k) f_j(\zeta_{\ell'})\end{aligned}$$

where $f_j(\zeta_{\ell'})$ denotes the action of the discretized $\delta\Lambda_\gamma^M$ matrix on the jth normalized basis function evaluated at $\zeta_{\ell'}$. Define

$$\widetilde{\mathbf{G}}_k(\ell, \ell') = \begin{cases} G_k(z_\ell, \zeta_{\ell'}) & \ell \neq \ell' \\ \frac{L}{P} \int_{E_{\ell'}} G_k(z_\ell - \zeta) dS(\zeta) & \ell = \ell' \end{cases} \quad (29)$$

then

$$\sum_{j=1}^{L-1} b_j^1(k)\Phi_\ell^j \approx \sum_{j=1}^{L-1} c_j^1(k)\Phi_\ell^j - \frac{P}{L}\sum_{j=1}^{L-1} b_j^1(k)\sum_{\ell'=1}^{L} \tilde{\mathbf{G}}_k(\ell,\ell')f_j(\zeta_{\ell'}). \quad (30)$$

Following [13]

$$f_p(\zeta_{\ell'}) \approx (\Phi\delta\Lambda_\gamma^M)(\ell', j) \quad (31)$$

i.e., the $(\ell',)$th entry in the matrix resulting from multiplication of the normalized current pattern matrix Φ and the discretized difference in DN maps $\delta\Lambda_\gamma^M$. Using the properties of matrix multiplication, (30) can be rewritten as

$$\sum_{j=1}^{L-1} b_j^1(k)\Phi_\ell^j = \sum_{j=1}^{L-1} c_j^1(k)\Phi_\ell^j - \frac{P}{L}\sum_{j=1}^{L-1} b_j^1(k)(\tilde{\mathbf{G}}_k\Phi\delta\Lambda_\gamma^M)(\ell, j)$$

or equivalently

$$\Phi\mathbf{b^1} = \Phi\mathbf{c^1} - \frac{P}{L}\tilde{\mathbf{G}}_k\Phi\delta\Lambda_\gamma^M\mathbf{b^1}$$

a matrix equation for the unknown coefficients $\mathbf{b^1}$ which are needed in the expansion of $\tilde{u}_1 = u_1 - 1/ik$.

Using the orthonormality of Φ, we multiply both sides of the equation by Φ^T, and solve

$$(I + A)\mathbf{b^1} = \mathbf{c^1}$$

where

$$A = \frac{P}{L}\Phi^T\tilde{\mathbf{G}}_k\Phi\delta\Lambda_\gamma^M. \quad (33)$$

For each value of $k \in \mathbb{C} \setminus \{0\}$, we solve the system (32) using GMRES for the unknown coefficients $\mathbf{b^1}$ and then reconstruct $u_1 - 1/ik$ for the specified value of k via (27).

Numerical experimentation has shown that the standard Green's function for the Laplacian

$$G_0(z-\zeta) := -\frac{1}{2\pi}\log|z-\zeta| \quad (34)$$

is a good approximation to $G_k(z-\zeta)$ [13], [39]. However, in [13], the singularity that occurs at $\zeta = z_\ell$ in G0 is dealt with by setting the value to zero. Here, we will instead use the more precise

calculation (29), replacing G_k by G_0, and calculate the integrable singularity numerically using Simpson's rule over the non-circular boundary $\partial\Omega$. For each subdivision E_ℓ, of the boundary

$$\int_{E_\ell} G_0(z_\ell - \zeta) dS(\zeta) \approx -\frac{1}{2\pi} \sum_{p=1}^{P_z} \log|z_\ell - \zeta_p|$$

where ζ_p, $p = 1, \ldots, P_z$, are points on E_ℓ such that no ζ_p coincides with z_ℓ.

Note that the boundary integral (9) for u_2 requires $G_0(-\overline{z} + \overline{\zeta})$ instead of $G_0(z - \zeta)$. Due to the definition of G_0 in (34), we have the relationship

$$G_0(z - \zeta) := -\frac{1}{2\pi} \log|z - \zeta| = G_0(-\overline{z} + \overline{\zeta}).$$

Therefore, in an analogous fashion, the unknown coefficients $\mathbf{b^2}$ for $\tilde{u}_2$ (using G_0) may be found via

$$(I + A)\mathbf{b^2} = \mathbf{c^2}$$

where A is the same matrix defined above in (33), and $\tilde{u}_2 = u_2 + 1/ik$ may be subsequently reconstructed via (27).

B. Computation of $\mathbf{\Psi_{12}}$ and $\mathbf{\Psi_{21}}$

To compute $\Psi_{12}(z, k)$ and $\Psi_{21}(z, k)$ for z on the boundary and $|k| \leq R$ from (14) and (15), only the coefficients in the expansions of $\tilde{u}_1(z, k)$ and $\tilde{u}_2(z, k)$ are needed. The ∂_z derivative of $G_k(-\overline{z} + \overline{\zeta})$ and $\overline{\partial}_z$ derivative of $G_k(z - \zeta)$ are approximated by $\partial_z G_k(-\overline{z}_n + \overline{\zeta}_{\ell'}) \approx \Gamma(n, \ell')$ where

$$\Gamma(n, \ell') \equiv \begin{cases} \frac{e^{i\overline{k}(z_n - \zeta_{\ell'})}}{4\pi(z_n - \zeta_{\ell'})}, & \text{if } \arg(z_n - \zeta_{\ell'}) \geq \text{tol} \\ 0, & \text{otherwise} \end{cases} \quad (36)$$

and $\partial^{-}{}_z G_k(z_n - \zeta_{\ell'}) \approx \tilde{\Gamma}(n, \ell')$ where

$$\tilde{\Gamma}(n, \ell') \equiv \begin{cases} \overline{\left[\frac{e^{ik(z_n - \zeta_{\ell'})}}{4\pi(z_n - \zeta_{\ell'})}\right]}, & \text{if } \arg(z_n - \zeta_{\ell'}) \geq \text{tol} \\ 0, & \text{otherwise} \end{cases} \quad (37)$$

respectively for $\ell' = 1, \ldots, L$ and $n = 1, \ldots, N_z$ where N_z is the number of evaluation points along the boundary. Note that N_z need not coincide with L. Now the vectors of CGO solutions Ψ_{12} and Ψ_{21} evaluated at N_z points on the boundary can be approximated by

$$\begin{aligned} \Psi_{12}(k) &\approx \frac{P}{N_z} \Gamma \Phi \delta \Lambda_\gamma^M \mathbf{b^2} \\ \Psi_{21}(k) &\approx \frac{P}{N_z} \tilde{\Gamma} \Phi \delta \Lambda_\gamma^M \mathbf{b^1}. \end{aligned} \quad (38)(39)$$

C. Computation of the Scattering Transforms

The formulas for the scattering transform $S_{12}(k)$ and $S_{21}(k)$, (23) and (24) respectively, require knowledge of the outward facing unit normal vector $\nu = (\nu_1, \nu_2) = \nu_1 + i\nu_2$ and its complex conjugate $\overline{\nu}$, respectively

$$S_{12}(k) = \frac{i}{2\pi}\int_{\partial\Omega} e^{-i\overline{k}z}\Psi_{12}(z,k)(\nu_1 + i\nu_2)dS(z)$$
$$S_{21}(k) = -\frac{i}{2\pi}\int_{\partial\Omega} e^{i\overline{k}\overline{z}}\Psi_{21}(z,k)(\nu_1 - i\nu_2)dS(z)$$

for each evaluation point z along the boundary. When the boundary is a circle of radius r, ν can be described by the coordinate z on $\partial\Omega$ divided by its magnitude (i.e., $z/|z|$). However, when the boundary is noncircular, as in the case with the chest-shaped domain used here, we must approximate ν using a parameterization $r(\theta)$ of the boundary for $\theta \in [0,2\pi)$.

Previous methods [40], [41] have transformed the problem to the unit disc by scaling the DN map by the maximum radial value of the noncircular domain and have produced good reconstructions. Here, as in [23], we seek to improve the reconstructions by a more accurate modeling of the boundary of the domain and thus do not scale the DN map by any radial component.

The unit outward normal vector at a point $z_0 = x_0 + iy_0$ on the boundary was approximated by setting $\nu(z_0)$ equal to the outward facing vector orthogonal to the unit tangent vector $\tau(z_0)$ to the boundary pointing in the counter-clockwise orientation in θ. This tangent vector was approximated by taking a forward difference with a second point z_+ on $\partial\Omega$ a small distance away from z_0 in the counter-clockwise direction

$$\tau(z_0) \approx \frac{(x_+ - x_0) + i(y_+ - y_0)}{\sqrt{(x_+ - x_0)^2 + (y_+ - y_0)^2}}$$

and therefore

$$\nu(z_0) \equiv \tau_2(z_0) - i\tau_1(z_0).$$

When evaluating the scattering transforms $S_{12}(k)$ and $S_{21}(k)$ numerically, we approximate the integral by a finite sum using a Simpson's rule as follows:

$$S_{12}(k) \approx \frac{i}{2\pi}\frac{P}{N_z}\sum_{n=1}^{N_z} e^{-i\overline{k}z_n}\Psi_{12}(z_n,k)\nu_n$$
$$S_{21}(k) \approx -\frac{i}{2\pi}\frac{P}{N_z}\sum_{n=1}^{N_z} e^{i\overline{k}\overline{z_n}}\Psi_{21}(z_n,k)\overline{\nu_n} \quad (40)(41)$$

and use bilinear interpolation to compute $S_{12}(0)$ and $S_{21}(0)$. The scattering transform is computed for $|k| \leq R$ and further restricted in the case of noisy data, which results in blow-up of the scattering transform. This truncation has been rigorously proven to be tantamount to a nonlinear

regularization for the D-bar method for real-valued conductivities [34], and it has the same regularizing behavior for this method.

D. Solution of the System of D-Bar Equations

The solution to the matrix $\overline{\partial}_k$ (20) can be written as two systems as follows:

$$\begin{cases} 1 = & M_{11}(z,k) - \frac{1}{\pi k} * (M_{12}(z,\overline{k})e(z,-k)S_{21}(k)) \\ 0 = & M_{12}(z,k) - \frac{1}{\pi k} * (M_{11}(z,\overline{k})e(z,\overline{k})S_{12}(k)) \end{cases} \quad (42)$$

and

$$\begin{cases} 1 = & M_{22}(z,k) - \frac{1}{\pi k} * (M_{21}(z,\overline{k})e(z,\overline{k})S_{12}(k)) \\ 0 = & M_{21}(z,k) - \frac{1}{\pi k} * (M_{22}(z,\overline{k})e(z,-k)S_{21}(k)) \end{cases} \quad (43)$$

where $e(z,k) = e^{i(zk+\overline{z}\overline{k})}$.

The numerical solver developed in [31] for the inverse conductivity problem for equations of the form

$$\overline{\partial}_k v(k) = T(k)\overline{v(k)}$$

was adapted to solve systems of equations and to take into account the difference that here the unknowns $M(z,k)$ are not conjugated, but instead the argument k is conjugated. The solver is based on the fast method by Vainikko [47] that uses FFT's for solving integral equations with weakly singular kernels. Here, we use a one-grid version of that method. The implementation for this problem is described in [24]. Note that (42) and (43) are solved for $|k| \leq R$.

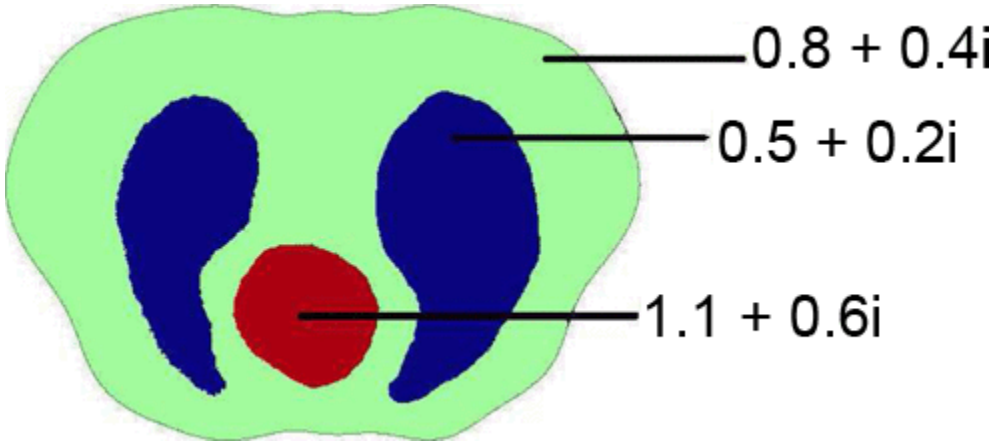

Fig. 2. Baseline phantom. Admittivity values are in $\mathrm{S/m}$.

The convolution $1/\pi k * f(k)$ is implemented with FFT's on a uniform k-grid of size $(2^N + 1) \times (2^N + 1)$ with uniform step size h_κ by computing

$$\frac{1}{\pi k} * f(k) = h_\kappa^2 \text{IFFT}(\text{FFT}(\frac{1}{\pi k})\text{FFT}(f(k))).$$

A matrix-free solution of the resulting system for each value of z was accomplished using GMRES. This step of the method can be implemented in parallel for each z in the chosen mesh of Ω and one only needs to store $M(z, 0)$.

E. Computation of the Admittivity

The admittivity is computed by solving (16) numerically. The functions M_+ and M_- in (17) and (18) were evaluated using the entries of $M(z, 0)$ recovered when solving the $\overline{\partial}_k$ equation as above. Centered finite differences with a uniform step size of $h_z \approx 0.0031$ were used to evaluate the $\overline{\partial}_z$ and ∂_z derivatives of M_+ and M_-, respectively. The convolution was then computed using FFT's as above

$$\gamma(z) = \exp(-2h_z^2 \text{IFFT}(\text{FFT}(\frac{1}{\pi z})\text{FFT}(\frac{\partial_z M_-(z, 0)}{M_+(z, 0)}))).$$

SECTION V.

Results and Discussion

The test problems were constructed to be simple simulations of organs and situations of interest in EIT thoracic imaging. Reconstructions were computed on a z-mesh of 128×128 elements with zero-mean Gaussisan random noise added to the voltage data at 0%, 0.01%, 0.05%, and 0.1% of the maximum voltage for that data set, as described in Section II. Each EIT system has its own noise level associated with it, and some are published, some are not. As an example, the ACT3 system has phase sensitive voltmeters with a published resolution of 1 part in 2^{16} (16 bits) for both the real and quadrature voltage components, which is equivalent to an SNR of 104 dB [9], [10]. This corresponds to less than 0.01% error in the voltage measurements. The system has a 1 in 12 bit voltmeter resolution for faster data acquision, which corresponds to a voltmeter precision of 0.024%. Another test described in [10] performed on each channel reports an absolute accuracy of 99.5%.

In the noise-free case, the CGO solutions and scattering transform were computed on a disk of radius $R = 40$ in the k-plane. In the presence of noise, an additional nonuniform truncation approach was used to remove artificial blowups in the scattering data resulting from the noisy data. In each case, if the magnitude of either the real or imaginary parts of the scattering data $S(k)$ exceeded a certain empirically determined threshold, the value was set to zero. In general, the maximal admissible $|k|$ became smaller as the noise level increased. We include the results from the best choice of admissible k here and do not include a thorough study of the effects of various R in the scope of this paper but point out that the choices of R and such empirical

thresholds are very intuitive when looking at plots of the scattering data (see [23] for such pictures).

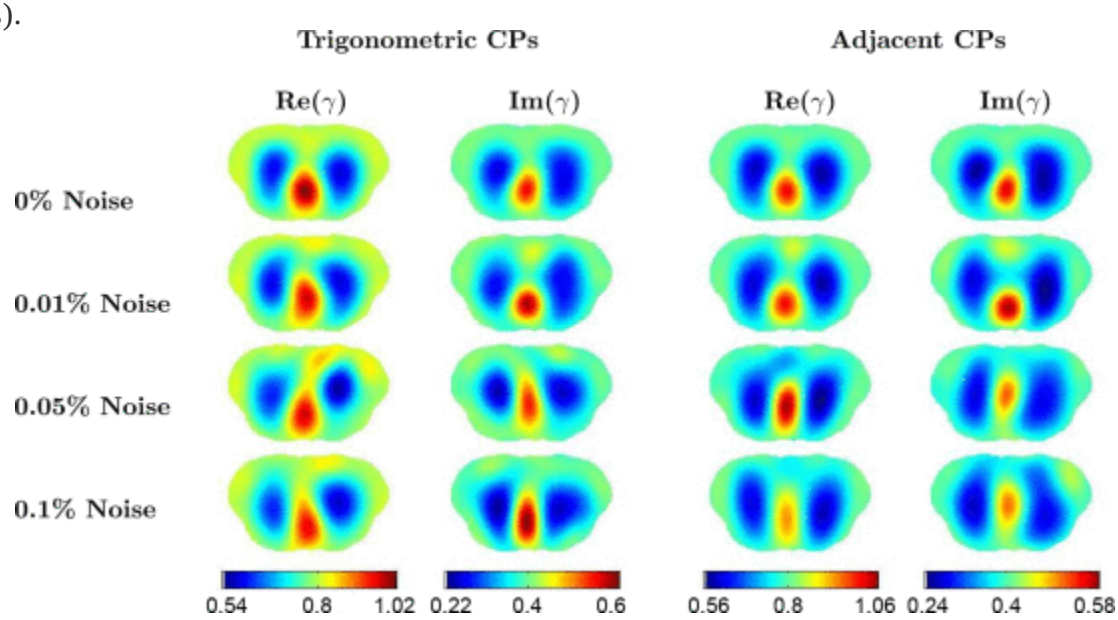

Fig. 3. Reconstructions of the baseline phantom using trigonometric and adjacent current patterns. Plots of the real and imaginary parts of the reconstruction are displayed on the same scale, respectively.

	Admittivity of test problem	0 % noise	0.01% noise	0.05% noise	0.1% noise
heart (TP)	$1.1 + 0.6i$	$1.02 + 0.56i$	$0.98 + 0.60i$	$0.98 + 0.55i$	$0.97 + 0.62i$
lungs (TP)	$0.5 + 0.2i$	$0.57 + 0.24i$	$0.57 + 0.25i$	$0.54 + 0.22i$	$0.56 + 0.22i$
dynamic range (TP)	N/A	σ: 76%, ϵ: 80%	σ: 69%, ϵ: 86%	σ: 74%, ϵ: 82%	σ: 68%, ϵ: 100%
heart (AP)	$1.1 + 0.6i$	$1.02 + 0.57i$	$1.02 + 0.59i$	$1.07 + 0.52i$	$0.94 + 0.51i$
lungs (AP)	$0.5 + 0.2i$	$0.57 + 0.24i$	$0.57 + 0.24i$	$0.55 + 0.27i$	$0.58 + 0.26i$
dynamic range (AP)	N/A	σ: 76%, ϵ: 80%	σ: 75%, ϵ: 87%	σ: 86%, ϵ: 63%	σ: 60%, ϵ: 64%

Table I Table Indicates Maximum Value of the Admittivity in the Heart Region and the Minimum Values of the Admittivity in the Lung Region in the Reconstructions for the Baseline Phantom with Trigonometric Current Patterns (TP) and Adjacent Current Patterns (AP). Actual Values are Provided for the Test Problem for Comparison. Dynamic Ranges for the Conductivity Images are Indicated by σ and for Permittivity by ϵ

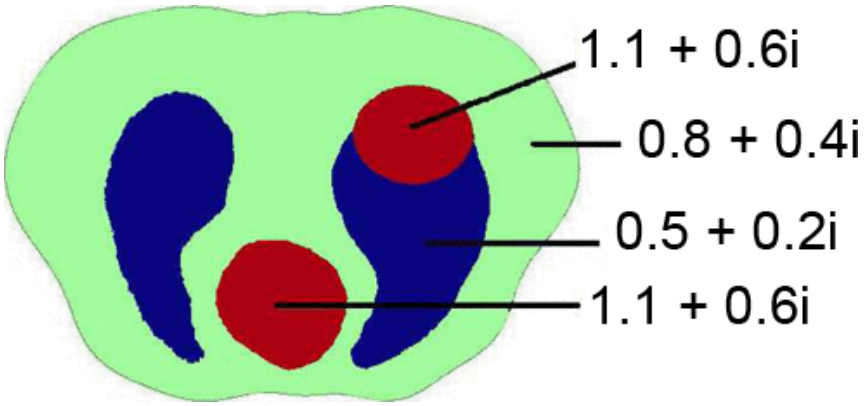

Fig. 4. The pleural effusion phantom. Admittivity values are in $\mathrm{S/m}$.

A. Baseline Data Set

The first example we consider is an idealized chest phantom with heart and lungs (see Fig. 2). The admittivity of the background was chosen to be $0.8 + 0.4iS/\mathrm{m}$, representing a rough average value of the low conductivity and permittivity components of bone and fat in a chest and the high conductivity and permittivity values of muscle. The admittivity of the heart was $1.1 + 0.6iS/\mathrm{m}$, and the admittivity of the lung was $0.5 + 0.2iS/\mathrm{m}$. Note that this example serves as a good baseline for the examples that follow that include additional inclusions or inhomogeneities.
Reconstructions of the baseline chest phantom from trigonometric and adjacent current patterns are found in Fig. 3. Recall from Section II that the current amplitude is $C = 2\mathrm{mA}$ and the effective contact impedance is $z = 10^{-8}\Omega/\mathrm{m}^2$. The reconstructions show excellent spatial resolution of the heart and lungs from noise-free data with a dynamic range of 76% for the conductivity and 80%

	Admittivity of test problem	0 % noise	0.01% noise	0.05% noise	0.1% noise
heart (TP)	$1.1 + 0.6i$	$1.05 + 0.58i$	$1.03 + 0.55i$	$1.01 + 0.57i$	$0.99 + 0.58i$
lungs (TP)	$0.5 + 0.2i$	$0.57 + 0.25i$	$0.59 + 0.23i$	$0.60 + 0.25i$	$0.58 + 0.27i$
pleural effusion (TP)	$1.1 + 0.6i$	$0.97 + 0.49i$	$0.93 + 0.53i$	$0.91 + 0.47i$	$0.90 + 0.47i$
dynamic range (TP)	N/A	σ: 79%, ϵ: 83%	σ: 74%, ϵ: 80%	σ: 70%, ϵ: 81%	σ: 70%, ϵ: 77%
heart (AP)	$1.1 + 0.6i$	$1.04 + 0.58i$	$1.05 + 0.57i$	$0.99 + 0.56i$	$0.96 + 0.60i$
lungs (AP)	$0.5 + 0.2i$	$0.57 + 0.24i$	$0.57 + 0.26i$	$0.59 + 0.25i$	$0.63 + 0.25i$
pleural effusion (AP)	$1.1 + 0.6i$	$0.97 + 0.49i$	$0.92 + 0.47i$	$0.88 + 0.48i$	$0.88 + 0.44i$
dynamic range (AP)	N/A	σ: 78%, ϵ: 83%	σ: 80%, ϵ: 77%	σ: 66%, ϵ: 79%	σ: 54%, ϵ: 87%

Table II Table Indicates the Maximum Value of the Admittivity in the Heart Region and in the Pleural Effusion Region and the Minimum Values of the Admittivity in the Lung Region in the Reconstructions for the Pleural Effusion Phantom with Trigonometric Current Patterns (TP) and Adjacent Current Patterns (AP). Actual Values are Provided for the Test Problem for Comparison. Dynamic Ranges for the Conductivity Images are Indicated by σ and for Permittivity by ϵ

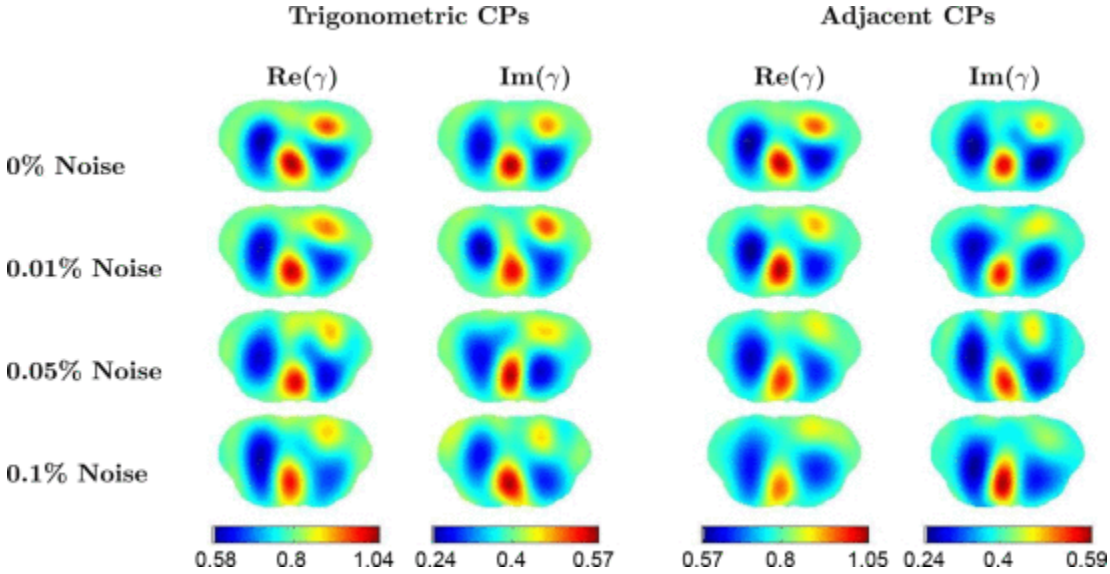

Fig. 5. Reconstructions of the pleural effusion phantom using trigonometric and adjacent current patterns. Plots of the real and imaginary parts of the reconstruction are displayed on the same scale, respectively.

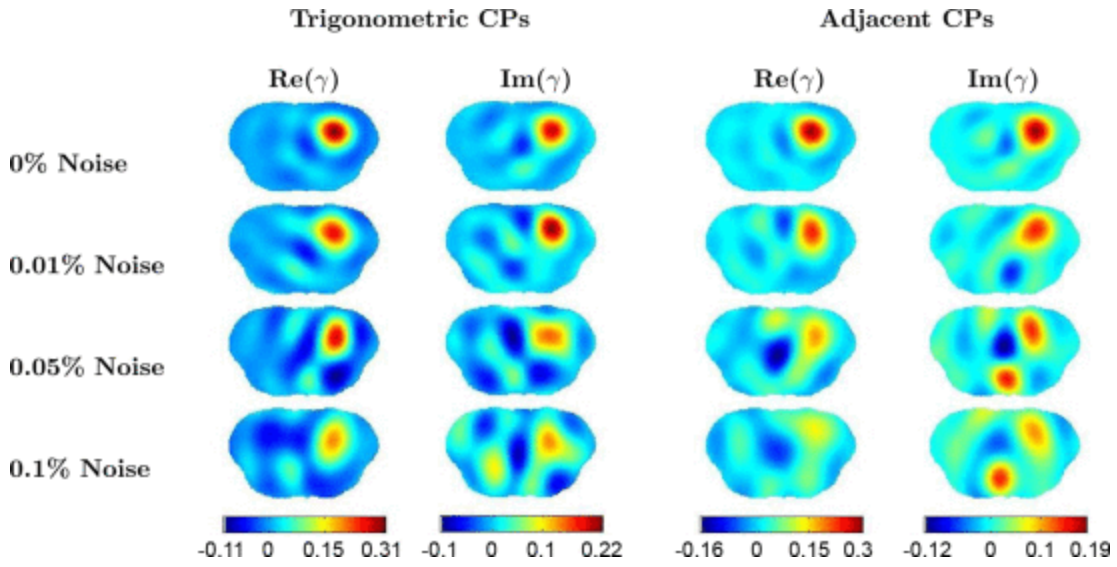

Fig. 6. Difference images produced by subtracting the baseline reconstructions in Fig. 3 from the pleural effusion reconstructions in Fig. 5. The real and imaginary parts are on the same respective scales. Note that the particular noise distribution is unique to each reconstruction, so subtraction does not remove these effects.

for the permittivity. The maximum value of the conductivity/permittivity was found in the heart region for all noise levels and correspondingly the minimum was found in the lung region. These values and values of the dynamic range are found in Table I for all noise levels for reconstructions from both sets of current patterns. With increasing noise level, there is an increasing distortion in the shape of the organ boundaries, and the heart appears elongated and pulled toward the center, particularly in the permittivity images from the adjacent current patterns.

B. Simulation of Pleural Effusion

A pleural effusion is a condition in which there is an excess of fluid in the pleural space, the area between the lung and chest cavity wall which naturally contains a small amount of lubricating fluid and layers of tissue. Pulmonary edema is characterized by fluid accumulation in the interstitial space of the lung, which may progress to accumulate in the alveoli in severe cases. The idealized numerical phantom presented here could serve as a model for either pleural effusion or focal edema in which the edema is not present throughout the entire lung. We will refer to this example as a pleual effusion for simplicity. The pleural effusion was simulated by adding a region of high conductivity, high permittivity in the left lung (see Fig. 4 and note that the subject's left lung appears on the right in the image), with conductivity and permittivity chosen to match that of the heart for simplicity, since this roughly simulates the electrical properties of blood. The dynamic ranges and the maximum and minimum reconstructed values for the heart, lungs, and fluid are shown Table II for the trigonometric and adjacent current patterns for the four noise levels considered here. In general, there is a decrease in dynamic range as the noise level increases. As is evident from the values in the table, and from the reconstructions in Fig. 5, the values in the fluid-filled region decrease with increasing noise, particularly for the adjacent current patterns. In general, however, the images are fairly robust with respect to noise, and the presence of an imhomogeneity is clearly visible in all images. As in the baseline image, there is some distortion of

the organs and the inhomogeneity with increasing noise level, and the heart is elongated, but is not pushed to the center as it was in the baseline images. Fig. 6 shows a difference image produced by subtracting the baseline reconstructions in Fig. 3 from the pleural effusion reconstructions in Fig. 5. The fluid-filled region is visible for all noise levels, and the spatial position is quite accurate for the lowest three levels. The contrast values diminish slightly with increasing noise level. The absolute images are arguably better than the difference images since the difference images contain artifacts due to organ distortion in the reconstructions. We remark that a new noise distribution was used in each reconstruction, so the effects of noise are not subtracted out in the difference images. This may be slightly contrary to the experimental case in which to some extent noise and electrode effects are subtracted out in difference images.

C. Simulations of Hyperinflation and Pneumothorax

	Admittivity of test problem	0 % noise	0.01% noise	0.05% noise	0.1% noise
heart (TP)	$1.1 + 0.6i$	$1.01 + 0.60i$	$1.03 + 0.59i$	$1.02 + 0.59i$	$1.02 + 0.50i$
lungs (TP)	$0.5 + 0.2i$	$0.56 + 0.22i$	$0.56 + 0.25i$	$0.55 + 0.24i$	$0.61 + 0.25i$
hyperinflation (TP)	$0.25 + 0.1i$	$0.50 + 0.22i$	$0.51 + 0.22i$	$0.51 + 0.23i$	$0.55 + 0.20i$
dynamic range (TP)	N/A	σ: 60%, ϵ: 75%	σ: 60%, ϵ: 74%	σ: 60%, ϵ: 72%	σ: 55%, ϵ: 60%
heart (AP)	$1.1 + 0.6i$	$1.02 + 0.60i$	$1.06 + 0.55i$	$0.97 + 0.61i$	$0.99 + 0.49i$
lungs (AP)	$0.5 + 0.2i$	$0.56 + 0.23i$	$0.60 + 0.25i$	$0.60 + 0.25i$	$0.63 + 0.27i$
hyperinflation(AP)	$0.25 + 0.1i$	$0.50 + 0.22i$	$0.52 + 0.22i$	$0.55 + 0.22i$	$0.57 + 0.25i$
dynamic range (AP)	N/A	σ: 60%, ϵ: 75%	σ: 63%, ϵ: 67%	σ: 50%, ϵ: 79%	σ: 49%, ϵ: 50%

Table III Table Indicates the Maximum Value of the Admittivity in the Heart Region and the MinimumValues of the Admittivity in the Lung and in the Hyperinflation Region in the Reconstructions for the Hyperinflation Phantom with Trigonometric Current Patterns (TP) and Adjacent Current Patterns (AP). The Dynamic Ranges for the Conductivity Images are Indicated by σ and for Permittivity by ϵ

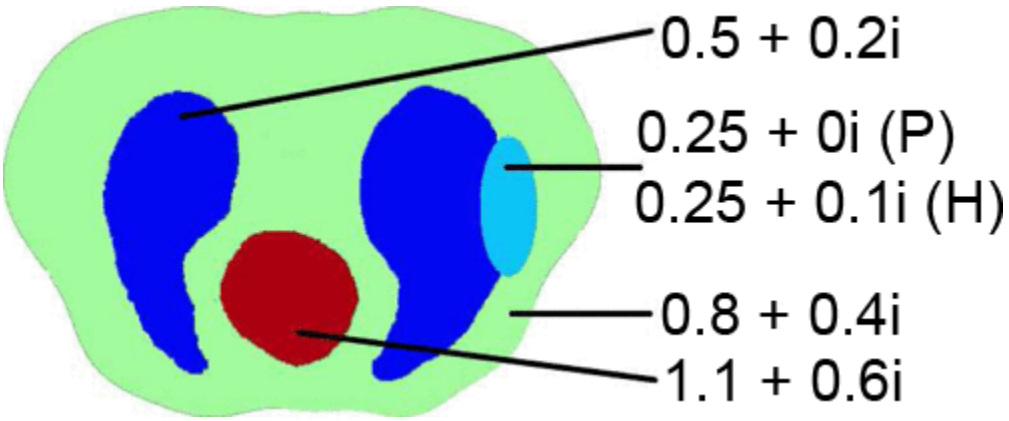

Fig. 7. Phantom for hyperinflation (H) and pneumothorax (P). Admittivity values are in S/m.

Hyperinflation in the left lung was simulated by adding a region of low conductivity and low permittivity to model the lower density of lung tissue in the left lung to the baseline phantom. A pneumothorax in the left lung was simulated by adding a region of low conductivity and zero permittivity in the left lung to the baseline phantom. The numerical phantoms for hyperinflation and pneumothorax are found in Fig. 7. The phantoms differ from each other only in the permittivity values in the hyperinflation/pneumothorax lung region.

The maximum and minimum values for the heart, lungs, and region of hyperinflation are shown in Table III for the trigonometric and adjacent current patterns. While there is little to no drop in the reconstructed values in this region, the reconstructions, found in Fig. 8 do show an enlarged left lung, particularly in permittivity images. To further study the reconstruction of this region, Fig.9shows a difference image produced by subtracting the baseline reconstructions in Fig. 3 from those for hyperinflation in Fig. 8. It is clear from the difference images, particularly in the noise-free case, that a region more resistive and with lower permittivity than the background is present near the left lung. However, other differences between the hyperinflation reconstruction and baseline are equally prominent in the difference image, and so identifying such a region from the difference image may also be inconclusive. However, the noise-free case and the absolute images show that the small difference in organ shape and conductivity values in the phantom does correspond to a reconstructable image by this method, and the method used here of modeling noise, namely, a unique noise distribution for each data set, does not perfectly correspond to an experimental situation, where the noise has a random component as well as a system-related component that does not change with each data set for a given experimental set-up. All data sets, including noise-free data, do contain contact impedance, modeled in the same way in each simulation.

The corresponding table of maximum and minimum values for the pneumothorax are shown in Table IV, and the absolute images are found in Fig. 10. The reconstructions again show an enlarged left lung, with good organ shape resolution and overall reconstructed conductivity values, but with no drop in the conductivity in the pneumothorax region. The difference images, found in Fig. 11, are comparable to those of hyperinflation. Finally, images formed by subtracting the hyperinflation reconstructions in Fig. 8 from the pneumothorax reconstructions in Fig. 10 are found in Fig. 12. These reconstructions show that for noise-free data the small difference in permittivity between the hyperinflation phantom and the pneumothorax phantom is clearly discernible. The results from noisy data are inconclusive due to the large discrepancies in organ boundaries that result in artifacts of similar magnitude to the small differences we are looking for here.

SECTION VI.

Conclusion

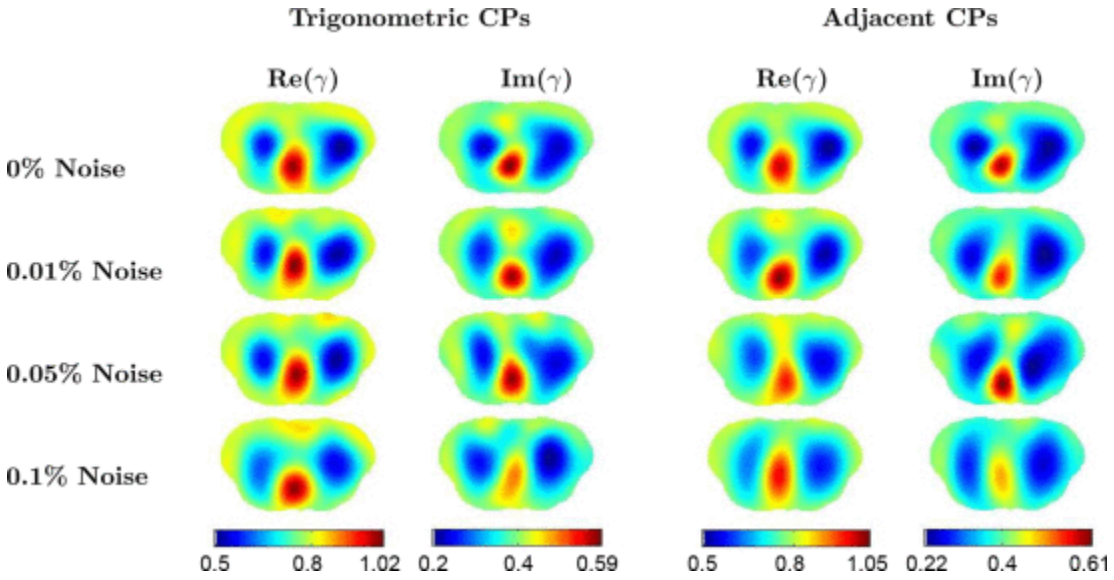

Fig. 8. Reconstructions of the hyperinflation phantom using trigonometric and adjacent current patterns. Plots of the real and imaginary parts of the reconstruction are displayed on the same scale, respectively.

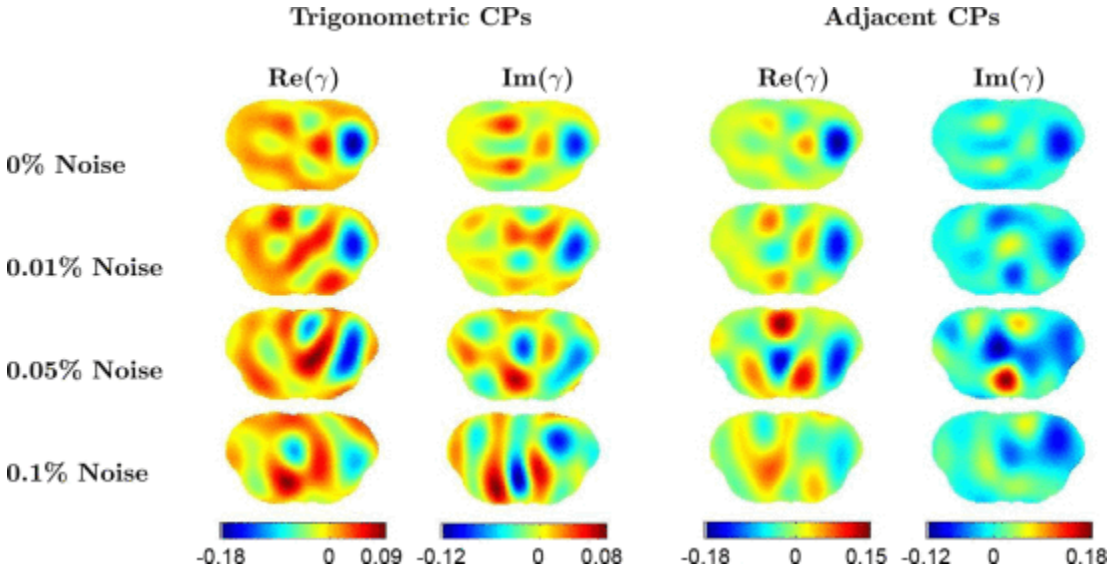

Fig. 9. Difference images at increasing noise levels produced by subtracting the baseline reconstructions in Fig. 3 from those for hyperinflation in Fig. 8. The real and imaginary parts are on the same respective scales. Note that the particular noise distribution is unique to each reconstruction, so subtraction does not remove these effects.

	Admittivity of test problem	0 % noise	0.01% noise	0.05% noise	0.1% noise
heart (TP)	$1.1 + 0.6i$	$1.01 + 0.59i$	$1.04 + 0.59i$	$1.03 + 0.59i$	$0.97 + 0.52i$
lungs (TP)	$0.5 + 0.2i$	$0.56 + 0.22i$	$0.56 + 0.25i$	$0.60 + 0.27i$	$0.60 + 0.26i$
pneumothorax (TP)	$0.25 + 0i$	$0.51 + 0.17i$	$0.50 + 0.16i$	$0.55 + 0.20i$	$0.54 + 0.21i$
dynamic range (TP)	N/A	σ: 59%, ϵ: 71%	σ: 64%, ϵ: 70%	σ: 58%, ϵ: 64%	σ: 51%, ϵ: 51%
heart (AP)	$1.1 + 0.6i$	$1.01 + 0.58i$	$1.02 + 0.59i$	$1.01 + 0.50i$	$0.99 + 0.54i$
lungs (AP)	$0.5 + 0.2i$	$0.56 + 0.22i$	$0.59 + 0.27i$	$0.59 + 0.28i$	$0.59 + 0.29i$
pneumothorax (AP)	$0.25 + 0i$	$0.51 + 0.17i$	$0.52 + 0.18i$	$0.53 + 0.19i$	$0.55 + 0.18i$
dynamic range (AP)	N/A	σ: 59%, ϵ: 70%	σ: 59%, ϵ: 69%	σ: 57%, ϵ: 50%	σ: 51%, ϵ: 60%

Table IV Table Indicates the Maximum Value of the Admittivity in the Heart Region and the the MinimumValues of the Admittivity in the Lung Region and in the Pneumothorax Region in the Reconstructions for the Pneumothorax Phantom with Trigonometric Current Patterns (TP) and Adjacent Current Patterns (AP). The Dynamic Ranges for the Conductivity Images are Indicated by σ and for Permittivity by ϵ

We have presented a direct 2-D EIT reconstruction algorithm for conductivity and permittivity on an arbitrary domain, and demonstrated that it provides reconstructions with very good spatial resolution on simulated data with low noise levels. It is demonstrated to be effective on pairwise current injection data with adjacent current patterns and on

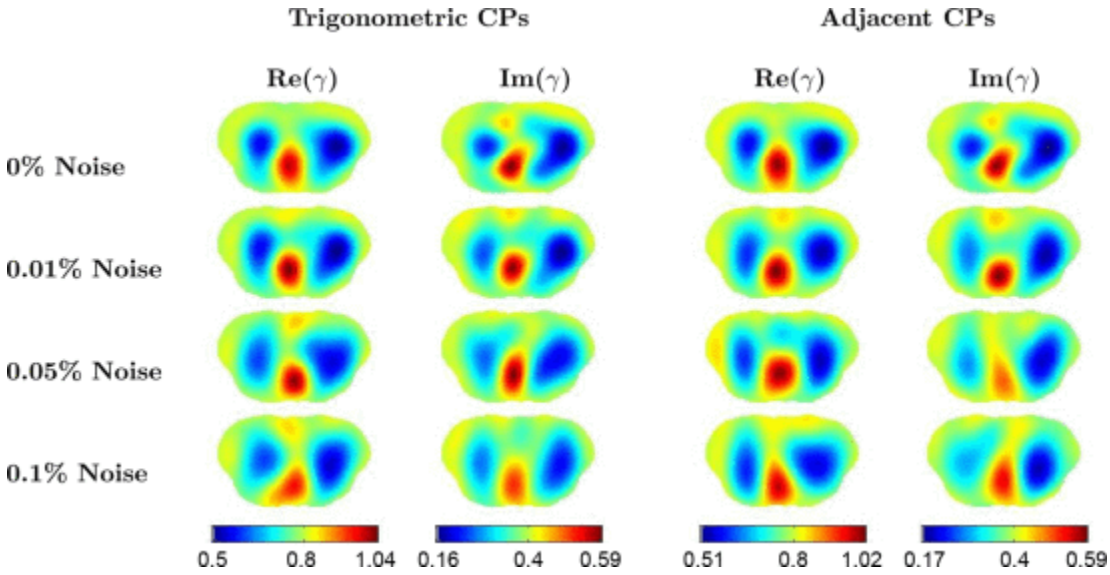

Fig. 10. Reconstructions of the pneumothorax phantom using trigonometric and adjacent current patterns. Plots of the real and imaginary parts of the reconstruction are displayed on the same scale, respectively.

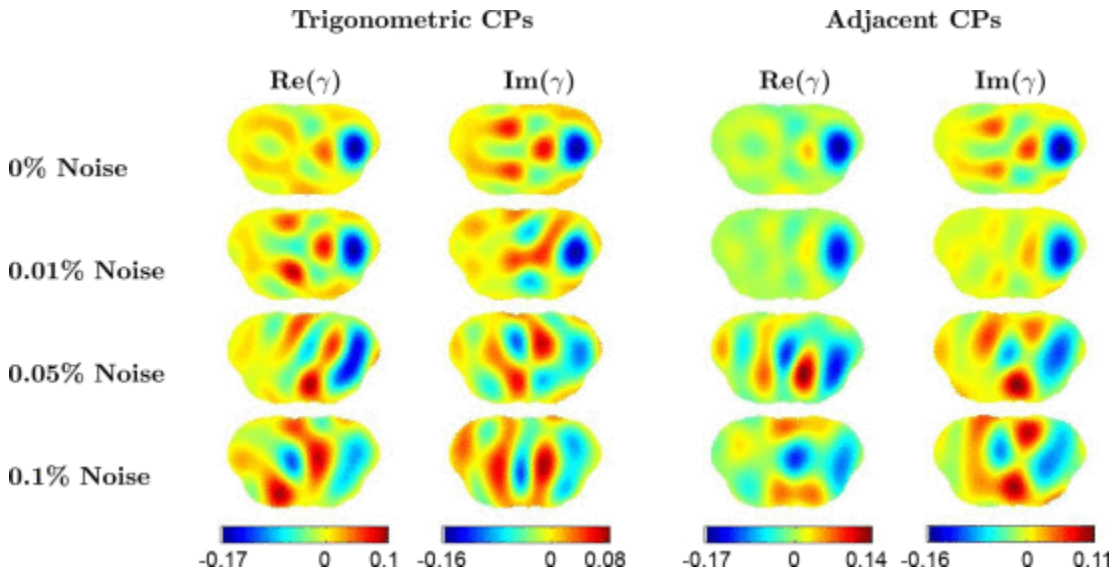

Fig. 11. Difference images produced by subtracting the baseline reconstructions in Fig. 3 from the pneumothorax reconstructions in Fig. 10. The real and imaginary parts are on the same respective scales. Note that the particular noise distribution is unique to each reconstruction, so subtraction does not remove these effects.

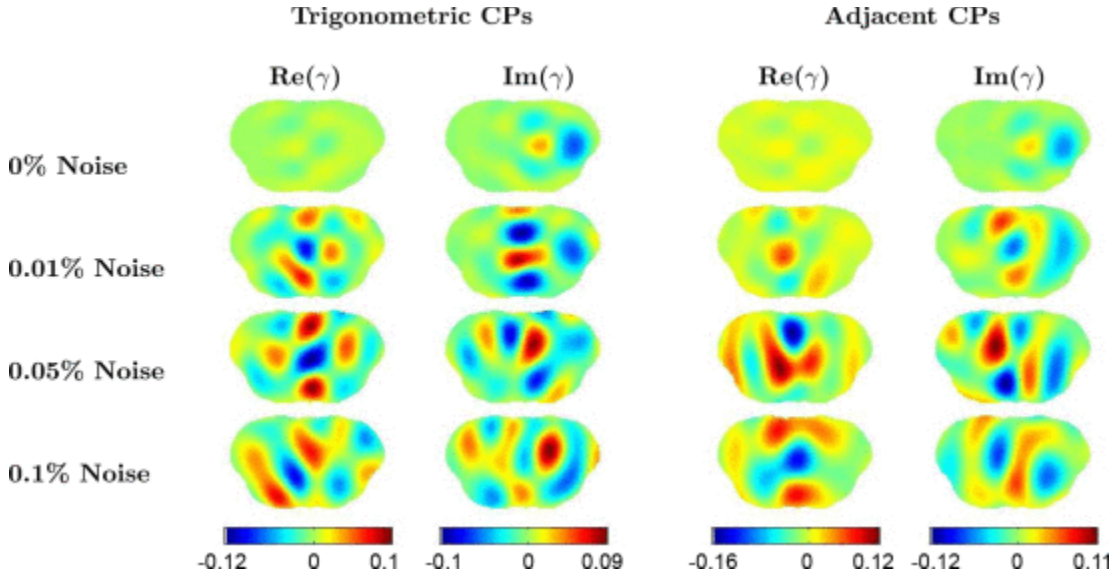

Fig. 12. Difference images produced by subtracting the hyperinflation reconstructions in Fig. 8 from the pneumothorax reconstructions in Fig. 10. The real and imaginary parts are on the same respective scales. Note that the particular noise distribution is unique to each reconstruction, so subtraction does not remove these effects.

trigonometric current pattern data. While the simulations presented here do not guarantee good results on experimental data, the good spatial resolution and reconstructed values on simulated chest phantoms including pleural effusion, hyperinflation, and pneumothorax indicate that the algorithm holds promise for applications to lung imaging. The difference images indicate the algorithm has the ability to distinguish between inhomogeneities with only a small difference in conductivity or permittivity values. The examples of hyperinflation and pneumthorax considered

here differed from each other only in the imaginary component and the difference was $0.1 S/m$ in the simulated phantom in a small region in the left lung. This difference was clearly apparent in the noise-free difference images between these two reconstructions.

References

1 A. Aghasi, M. Kilmer, E. L. Miller, "Parametric level set methods for inverse problems", *SIAM J. Imag. Sci.*, vol. 1, pp. 618-650, 2011.

2 K. Astala, J. L. Mueller, L. Pivrinta, A. Permki, S. Siltanen, "Direct electrical impedance tomography for nonsmooth conductivities", *Inverse Problems Imag.*, vol. 5, pp. 531-550, 2011.

3 L. Borcea, "Electrical impedance tomography", *Inverse Problems*, vol. 18, pp. 99-136, 2002.

4 Boverman, T.-J. Kao, R. Kulkarni, B. S. Kim, D. Isaacson, G. J. Saulnier, J. C. Newell, "Robust linearized image reconstruction for multifrequency EIT of the breast", *IEEE Trans. Biomed. Eng.*, vol. 27, no. 10, pp. 1439-1448, Oct. 2008.

5 B. H. Brown, D. C. Barber, A. H. Morice, A. Leathard, A. Sinton, "Cardiac and respiratory related electrical impedance changes in the human thorax", *IEEE Trans. Biomed. Eng.*, vol. 41, no. 8, pp. 729-734, Aug. 1994.

6 M. Brhl, M. Hanke, "Numerical implementation of two non-iterative methods for locating inclusions by impedance tomography", *Inverse Problems*, vol. 16, pp. 1029-1042, 2000.

7 K.-. S. Cheng, D. Isaacson, J. C. Newell, D. G. Gisser, "Electrode models for electric current computed tomography", *IEEE Trans. Bio. Eng.*, vol. 36, no. 9, pp. 918-924, Sep. 1989.

8 E. T. Chung, T. F. Chan, X.-C. Tai, "Electrical impedance tomography using level set representation and total variation regularization", *J. Comp. Phys.*, vol. 205, pp. 357-372, 2005.

9 R. D. Cook, G. J. Saulnier, J. C. Goble, "A phase sensitive voltmeter for a high-speed high precision electrical impedance tomograph", *Proc. Ann. Int. Conf. IEEE Eng. Med. Biol. Soc.*, pp. 22-23, 1991.

10 R. D. Cook, G. J. Saulnier, D. G. Gisser, J. C. Goble, J. C. Newell, D. Isaacson, "Act3: A high-speed high precision electrical impedance tomograph", *IEEE Trans. Biomed. Eng.*, vol. 41, no. 8, pp. 713-722, Aug. 1994.

11 E. L. V. Costa, C. N. Chaves, S. Gomes, R. G. Lima, M. B. P. Amato, "Real-time detection of pneumothorax using electrical impedance tomography", *Crit. Care Med.*, vol. 36, pp. 1230-1238, 2008.

12 E. L. V. Costa, R. G. Lima, M. B. P. Amato, "Electrical impedance tomography", *Current Opin. Crit. Care*, vol. 15, pp. 18-24, 2009.

13 M. DeAngelo, J. L. Mueller, "D-bar reconstructions of human chest and tank data using an improved approximation to the scattering transform", *Physiological Meas.*, vol. 31, pp. 221-232, 2010.

14 O. Dorn, D. Lesselier, "Level set methods for inverse scattering", *Inverse Problems*, vol. 22, pp. R67-R67, 2006.

15 P. M. Edic, D. Isaacson, G. J. Saulnier, H. Jain, J. C. Newell, "An iterative Newton-Raphson method to solve the inverse admittivity problem", *IEEE Trans. Biomed. Eng.*, vol. 45, no. 7, pp. 899-908, Jul. 1998.

16 L. D. Faddeev, "Increasing solutions of the Schrödinger equation", *Sov. Phys. Dokl.*, vol. 10, pp. 1033-1035, 1966.

17 E. Francini, "Recovering a complex coefficient in a planar domain from the Dirichlet-to-Neumann map", *Inverse Problems*, vol. 6, pp. 107-119, 2000.

18 D. Freimark, M. Arad, R. Sokolover, S. Zlochiver, S. Abboud, "Monitoring lung fluid content in CHF patients under intravenous diuretics treatment using bio-impedance measurements", *Physiol. Meas.*, vol. 28, pp. S269-S277, 2007.

19 I. Frerichs, J. Hinz, P. Herrmann, G. Weisser, G. Hahn, T. Dudykevych, M. Quintel, G. Hellige, "Detection of local lung air content by electrical impedance tomography compared with electron beam CT", *J. Appl. Physiol.*, vol. 93, no. 2, pp. 660-6, 2002.

20 I. Frerichs, J. Hinz, P. Herrmann, G. Weisser, G. Hahn, M. Quintel, G. Hellige, "Regional lung perfusion as determined by electrical impedance tomography in comparison with electron beam CT imaging", *IEEE Trans. Med. Imag.*, vol. 21, no. 6, pp. 646-652, Jun. 2002.

21 I. Frerichs, G. Schmitz, S. Pulletz, D. Schdler, G. Zick, J. Scholz, N. Weiler, "Reproducibility of regional lung ventilation distribution determined by electrical impedance tomography during mechanical ventilation", *Physiol. Meas.*, vol. 28, pp. 261-267, 2007.

22 L. F. Fuks, M. Cheney, D. Isaacson, D. G. Gisser, J. C. Newell, "Detection and imaging of electric conductivity and permittivity at low frequency", *IEEE Trans. Biomed. Eng.*, vol. 38, no. 11, pp. 1106-1110, Nov. 1991.

23 S. J. Hamilton, *A direct D-bar reconstruction algorithm for complex admittivities in for the 2-D EIT problem*, Colorado State Univ., 2012.

24 S. J. Hamilton, C. N. L. Herrera, J. L. Mueller, A. V. Herrmann, "A direct D-bar reconstruction algorithm for recovering a complex conductivity in 2-D", *Inverse Problems*, vol. 28, pp. 095005, 2012.

25 M. Ikehata, "Reconstruction of the support function for inclusion from boundary measurements", *J. Inverse Ill-Posed Problems*, vol. 8, pp. 367-378, 2000.

26 M. Ikehata, S. Siltanen, "Numerical method for finding the convex hull of an inclusion in conductivity from boundary measurements", *Inverse Problems*, vol. 16, pp. 1043-1052, 2000.

27 D. Isaacson, M. Cheney, "Current problems in impedance imaging" in Inverse Problems in Parital Differential Equations, PA, Philadelphia:SIAM, pp. 139-148, 1990.

28 D. Isaacson, J. L. Mueller, J. C. Newell, S. Siltanen, "Reconstructions of chest phantoms by the D-bar method for electrical impedance tomography", *IEEE Trans. Med. Imag.*, vol. 23, no. 7, pp. 821-828, Jul. 2004.

29 D. Isaacson, J. L. Mueller, J. C. Newell, S. Siltanen, "Imaging cardiac activity by the D-bar method for electrical impedance tomography", *Physiol. Meas.*, vol. 27, pp. S43-S50, 2006.

30 H. Jain, D. Isaacson, P. M. Edic, J. C. Newell, "Electrical impedance tomography of complex conductivity distributions with noncircular boundary", *IEEE Trans. Biomed. Eng.*, vol. 44, no. 11, pp. 1051-1060, Nov. 1997.

31 K. Knudsen, J. L. Mueller, S. Siltanen, "Numerical solution method for the D-bar-equation in the plane", *J. Comp. Phys.*, vol. 198, pp. 500-517, 2004.

32 K. Knudsen, M. Lassas, J. L. Mueller, S. Siltanen, "Reconstructions of piecewise constant conductivities by the D-bar method for electrical impedance tomography", *Proc. 4th AIP Int. Conf. 1st Congress IPIA J. Physics: Conf. Ser.*, vol. 124, pp. 012029, 2008.

33 K. Knudsen, M. Lassas, J. L. Mueller, S. Siltanen, "D-bar method for electrical impedance tomography with discontinuous conductivities", *SIAM J. Appl. Math.*, vol. 67, pp. 893-913, 2007.

34 K. Knudsen, M. Lassas, J. L. Mueller, S. Siltanen, "Regularized D-bar method for the inverse conductivity problem", *Inverse Problems Imag.*, vol. 3, pp. 599-624, 2009.

35 P. W. Kunst, A. V. Noordegraaf, O. S. Hoekstra, P. E. Postmus, P. M. de Vries, "Ventilation and perfusion imaging by electrical impedance tomography: A comparison with radionuclide scanning", *Physiol. Meas.*, vol. 19, no. 4, pp. 481-90, 1998.

36 P. W. Kunst, A. V. Noordegraaf, E. Raaijmakers, J. Bakker, A. B. Groeneveld, P. E. Postmus, P. M. de Vries, "Electrical impedance tomography in the assessment of extravascular lung water in noncardiogenic acute respiratory failure", *Chest*, vol. 116, pp. 1695-1702, 1999.

37 J. L. Mueller, S. Siltanen, Linear and Nonlinear Inverse Problems With Practical Applications, PA, Philadelphia:SIAM, 2012.

38 J. L. Mueller, S. Siltanen, D. Isaacson, "A direct reconstruction algorithm for electrical impedance tomography", *IEEE Trans. Med. Imag.*, vol. 21, no. 6, pp. 555-559, Jun. 2003.

39 J. L. Mueller, S. Siltanen, "Direct reconstructions of conductivities from boundary measurements", *SIAM J. Sci. Comp.*, vol. 24, pp. 1232-1266, 2003.

40 E. Murphy, J. L. Mueller, J. C. Newell, "Reconstruction of conductive and insulating targets using the D-bar method on an elliptical domain", *Physiol. Meas.*, vol. 28, pp. S101-S114, 2007.

41 E. K. Murphy, J. L. Mueller, "Effect of domain-shape modeling and measurement errors on the 2-D D-bar method for electrical impedance tomography", *IEEE Trans. Med. Imag.*, vol. 28, no. 10, pp. 1576-1584, Oct. 2009.

42.

N. Polydorides, W. R. B. Lionheart, "A MATLAB toolkit for three-dimensional electrical impedance tomography: A contribution to the electrical impedance and diffuse optical reconstruction software project", *Meas. Sci. Tech.*, vol. 13, pp. 1871, 2002.

43 S. Siltanen, J. Mueller, D. Isaacson, "An implementation of the reconstruction algorithm of a. nachman for the 2-D inverse conductivity problem", *Inverse Problems*, vol. 16, pp. 681-699, 2000.

44 H. Smit, A. V. Noordegraaf, J. T. Marcus, A. Boonstra, P. M. de Vries, P. E. Postmus, "Determinants of pulmonary perfusion measured by electrical impedance tomography", *Eur. J. Appl. Physiol.*, vol. 92, pp. 45-49, 2004.

45 E. Somersalo, M. Cheney, D. Isaacson, "Existence and uniqueness for electrode models for electric current computed tomography", *SIAM J. Appl. Math.*, vol. 52, no. 4, pp. 1023-1040, 1992.

46 S. Siltanen, J. P. Tamminen, "Reconstructing conductivities with boundary corrected D-bar method", *J. Inverse Ill-posed Problems*.

47 G. Vainikko, "Fast solvers of the Lippmann-Schwinger equation" in Direct and Inverse Problems of Mathematical Physics, MA, Norwell:Kluwer, vol. 5, pp. 423-440, 2000.

48 P. J. Vauhkonen, M. Vauhkonen, T. Savolainen, J. P. Kaipio, "Three-dimensional electrical impedance tomography based on the complete model", *IEEE Trans. Biomed. Eng.*, vol. 46, no. 9, pp. 1150-1160, Sep. 1999.

49 J. A. Victorino, J. B. Borges, V. N. Okamoto, G. F. J. Matos, M. R. Tucci, M. P. R. Caramez, H. Tanaka, D. C. B. Santos, C. S. V. Barbas, C. R. R. Carvalho, M. B. P. Amato, "Imbalances in Regional Lung ventilation: A validation study on electrical impedance tomography", *Am. J. Respir. Crit. Care Med*, vol. 169, pp. 791-800, 2004.

50 A. V. Herrmann, *Properties of the reconstruction algorithm and associated scattering transform for admittivity in the plane*, Colorado State Univ., 2009.